Journal of Mining and Environment (JME), Vol. 14, No. 4, 2023, 1239-1260

Shahrood University of Technology

Journal of Mining and Environment (JME)

Journal homepage: www.jme.shahroodut.ac.ir

Iranian Society of Mining Engineering (IRSME)

A Predictive GIS Model for Mapping Gold and Copper-bearing Alteration zones at South Gabal Um Monqul and Gabal Al Kharaza Prospects, North Eastern Desert, Egypt

Abdallah Atef[1]*, Ahmed Ali Madani[1] , Adel Abdolallah Surour[1,2] and Mokhles Kamal Azer[3]

1. Department of Geology, Faculty of Science, Cairo University, Giza, Egypt
2. Department of Geological Sciences, Faculty of Science, Galala University, New Galala City, Egypt
3. Department of Geological Sciences, National Research Centre, Giza, Dokki, Egypt

Article Info

Received 27 July 2023
Received in Revised form 26 August 2023
Accepted 14 September 2023
Published online 14 September 2023

DOI: 10.22044/jme.2023.13406.2473

Keywords

Remote sensing
GIS analysis
Gold and copper mineralizations
Favorability maps
Knowledge-driven method

Abstract

This study reports the application of remote sensing data and knowledge-driven GIS modeling to provide favorability maps for gold and copper mineralized areas. The South Gabal Um Monqul (SGUM) and the Gabal Al Kharaza (GKZ) prospects located in the northern Eastern Desert of Egypt are the targets for the present study. Four thematic layers (lithology maps, old trenches buffer analysis, lineament density maps, and alteration zone maps) were prepared and used as inputs for a weighted overlay GIS model. Combined results from false color composite images, particularly the RGB parameters (PC2, PC1, and PC3) and the RGB parameters (MNF1, MNF2, and MNF3) classified the host rocks in both prospects. PCA-based extraction of lineaments was considered using line algorithm of PCI Geomatica. QuickBird band math (G+B), (R+G), and (G-B) for RGB was successful in delineating ancient workings within the mineralized zones. Old trenches layers were buffered to 20 m wide bands extending in all directions. Landsat-8 band ratios imagery (6/5 * 4/5, 6/7, and 6/2) in red, green, and blue (RGB) is potent in defining alteration zones that host gold and copper mineralizations. Acceptable scores of 30%, 30%, 20%, and 20% were assigned for the alteration zone maps, ancient workings buffer analysis, lithology maps and lineament density maps, respectively. Two favorability maps for mineralizations were generated for the SGUM and GKZ prospects. Validation of these maps and their potential application to detect new mineralization sites in the northern Eastern Desert were discussed.

1. Introduction

Detecting and mapping hydrothermal alteration zones are complex processes. However, remote sensing together with Geographic Information System (GIS) are effective techniques for mapping geological structures and locating hydrothermal alteration zones that may host mineralizations. Thus, these techniques were used to generate mineral exploration models for areas of high potentialities for various metals. Remote sensing and GIS techniques have been proven to be very successful in detecting and mapping hydrothermal alteration zones associated with gold-copper mineralizations [1–8].

In Egypt, some workers [9–19] utilized the Landsat Thematic Mapper (TM), Enhanced Thematic Mapper Plus (ETM+), Operational Land Imager (OLI), and the Advanced Spaceborne Thermal Emission/Reflection Radiometer (ASTER) imageries for lithological discrimination. Such techniques are powerful enough to identify and to delineated precisely gold-bearing alteration zones in the Arabian-Nubian Shield (ANS), which is known for his high potentiality for gold mineralizations as well as the Eastern Desert that represent the northwestern extension of the shield [6, 9, 12, 16, 17].

✉ *Corresponding author: abdallah@sci.cu.edu.eg (A. Atef)*

Utilization of GIS as a tool for mineral exploration is based on its capability to combine, integrate, manage, and analyze multi-spatial layers to get a GIS-based prediction model. Knowledge-driven and data-driven GIS models have been utilized to integrate multiple data for mapping and delineating favorable areas for promising mineral exploration programs [20-25]. Data-driven approaches involve quantitative analysis of data-rich concessions with various known mineral occurrences used as training samples in model training [22, 24, 25]. In contrast, knowledge-driven methods are used in poorly explored concessions where mineral occurrences are scarce [23, 25]. No training samples are required in knowledge-driven methods [22, 23, 25]. The choice of using data-driven or knowledge-driven approaches depends mainly on the availability of exploration data [22]. knowledge-driven method is the best scenario used in the current study depending on the quality of available data.

The majority of gold deposits in the ANS are structurally controlled. They are related to shear zones that host gold-bearing quartz veins and alteration zones [2٦]. Gold occurrences in the north Eastern Desert (NED) are not frequently recognized compared to the Central Eastern Desert (CED) and South Eastern Desert (SED) (Figure1a). The South Gabal Um Monqul (SGUM) and the Gabal Al Kharaza (GKZ) prospects were exploited for gold and copper from the Pre-dynastic Period (ca. 3000 BC) until the Arab time (ca. 1350 AD) [2٧, 28]. In the NED, the SGUM prospect area is located at the southeastern part of the Ras Gharib segment whereas the GKZ prospect area occupies the central part of the southwest Gabal Dara environ (Figure 1). The SGUM area covers approximately 20.2 km^2 that lies between latitudes 27°47’40” to 27°49’21” N, and longitudes 33°02’48” to 33°05’38” E. The GKZ area covers approximately 6.3 km^2 that lies between latitudes from 27°54’07” to 27°55’8” N and longitudes from 32°50’44” to 33°52’30” E. The current study presents a regional prediction model (PM) to define promising occurrences of gold and copper mineralizations for further exploration not only at the SGUM and GKZ prospects but also for the Precambrian basement rocks of the ANS and other arid terrains.

2. Geologic Setting and Host Rocks of Mineralizations

Neoproterozoic rocks in the NED remarkably differ from those in the CED and SED. In the NED, there are no records of Tonian-Cryogenian ophiolite sections or ophiolitic mélanges but it includes the Ediacaran island arc assemblages of the Dokhan volcanic series, voluminaous granitoids, and the Hammamat sediments (Figure 1c) [27, 29-37]. According to [35], the SGUM prospect area is occupied mainly by monzogranite, which is the main rock type in the majority of outcrops, with lesser amount of the Dokhan volcanics and fresh gabbro. This gabbro has an age of 603 ± 3.5 Ma [35]. The gabbro shows low to moderate relief, and the intrusion is represented by a few scattered and detached masses. It is melanocratic and varies in color from dark gray to grayish green. Sometimes, the color becomes lighter due to the relative proportion of mafic to felsic minerals, i.e. mesocratic. In comparison with the volume of the Dokhan volcanics and monzogranite, the gabbro is the least abundant and is restricted only to a few limited locations in the western extreme of the SGUM area. The Dokhan volcanics in the SGUM area are well-exposed at the entrance of the prospect covering its northwestern extreme. They are represented mainly by dacite and rhyodacite, which are fine-grained and some varieties show porphyritic texture. The age of the Dokhan volcanics in the SGUM area is a matter of debate. The volcanic rocks in the SGUM prospect are considered as the southern expression of the Dokhan Volcanics of Gabal Monqul [29, 30], which is dated as 618 Ma by [32]. Recently, LA-ICPMS U-Pb zircon age of 773 ± 6.9 Ma were assigned for the SGUM volcanics [35]. Considerable volumes of these volcanics were mapped as granodiorite by [33] (Figure 1c).

Granite covers more than half of the rock volume in the SGUM area. It hosts numerous pits that were excavated during ancient times, which dated back to the dynastic and Arab eras (Figure 2a). The granites are represented by syenogranite and monzogranite. The granites occur commonly as low-lying hillocks and as rugged hills of moderate elevation. It has pink to red color due to the predominance of feldspars. In some instances, the color becomes gray with common brownish desert varnish. In the hand specimen, the granite is medium- to coarse-grained, equigranular with some dispersed coarse feldspar crystals (up to 1.7 cm long) exhibiting porphyritic appearance. The granite in the SGUM area was locally sheared, and these shear zones were invaded by Fe-dominated mineralizing fluids containing appreciable Au, Cu, and Ba contents (Figure 2b). These shear zones (Figure 2c), and fractures exhibit different trends

and various thicknesses. The granite is altered along joints and fracture planes and dissected by mafic dikes of basaltic composition. In the present study, new remote sensing data (to be discussed in the following sections, and based on Figures 5 and 6) were utilized to obtain a modified geological map of the SGUM area (Figure 6a).

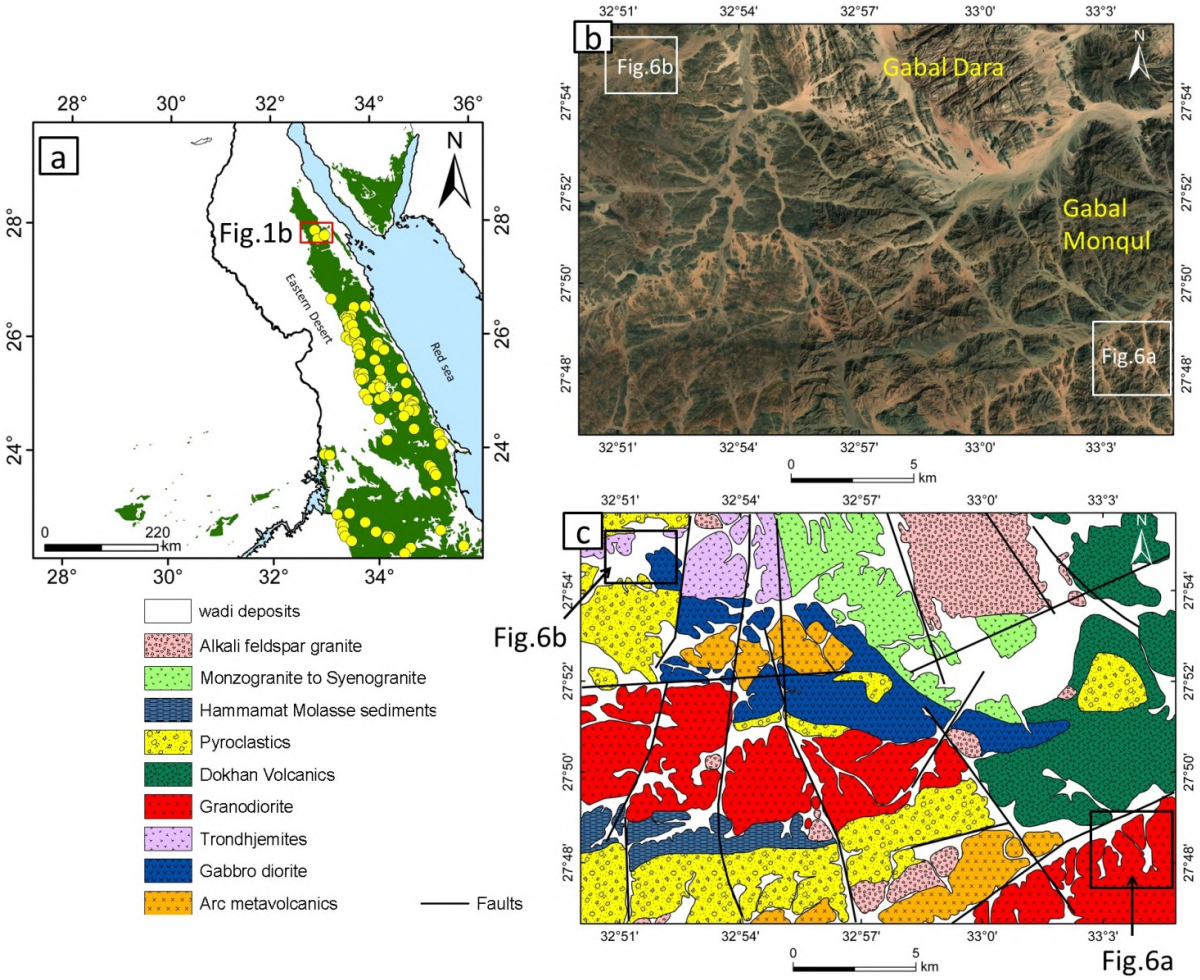

Figure 1. a) Location map of the studied district (red rectangle). Outlines of the Neoproterozoic Nubian Shield are shown in green. The yellow circles represent the gold occurrences in the Eastern Desert of Egypt after [38]. b) Google Earth image for the studied district in the NED. The white rectangles define the SGUM and GKZ prospects. c) Geological map of the Ras Gharib segment in the NED modified after [33]. The black rectangles define the locations of the SGUM and GKZ prospects.

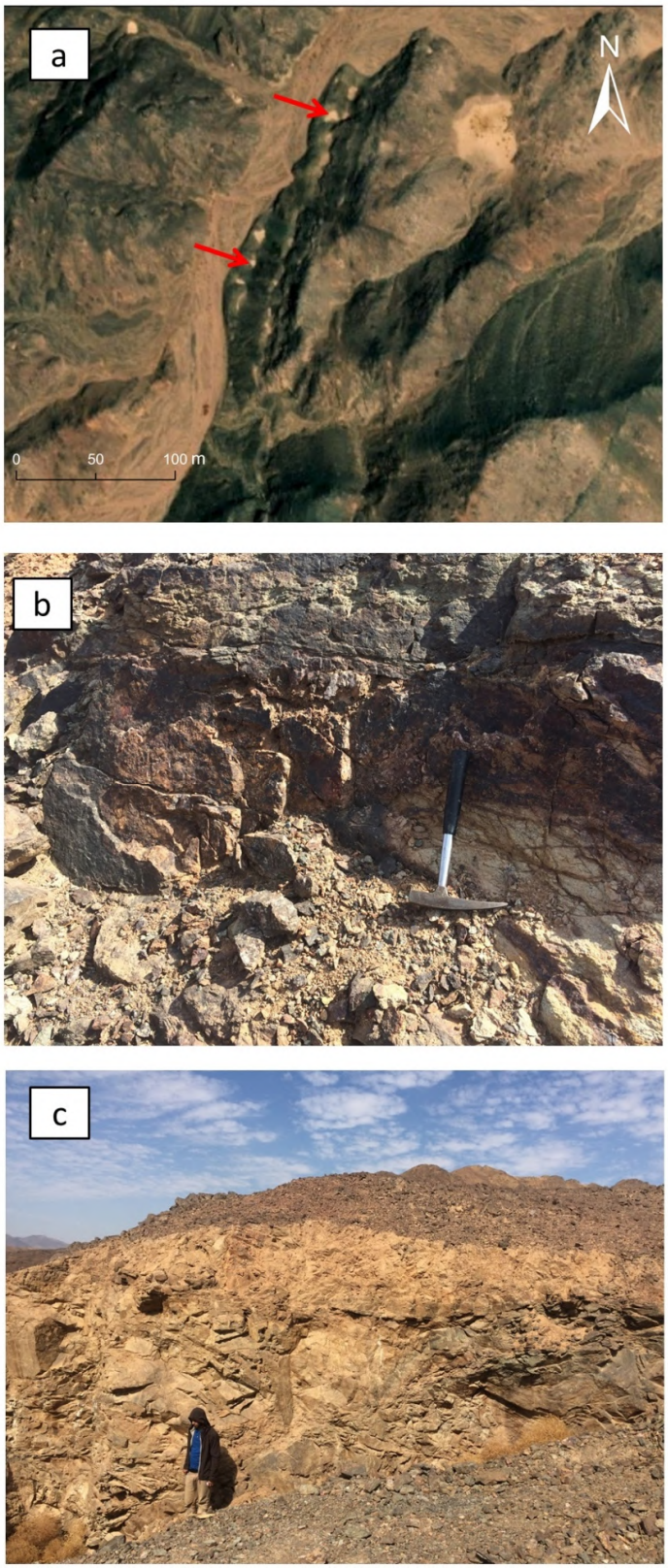

Figure 2. a) Satellite image showing the ancient mining activities following a NE-SW direction at the SGUM (marked by the red arrows). b) Fe-rich alteration zone within the monzogranite of the SGUM prospect. c) Sheared monzogranite at the SGUM prospect.

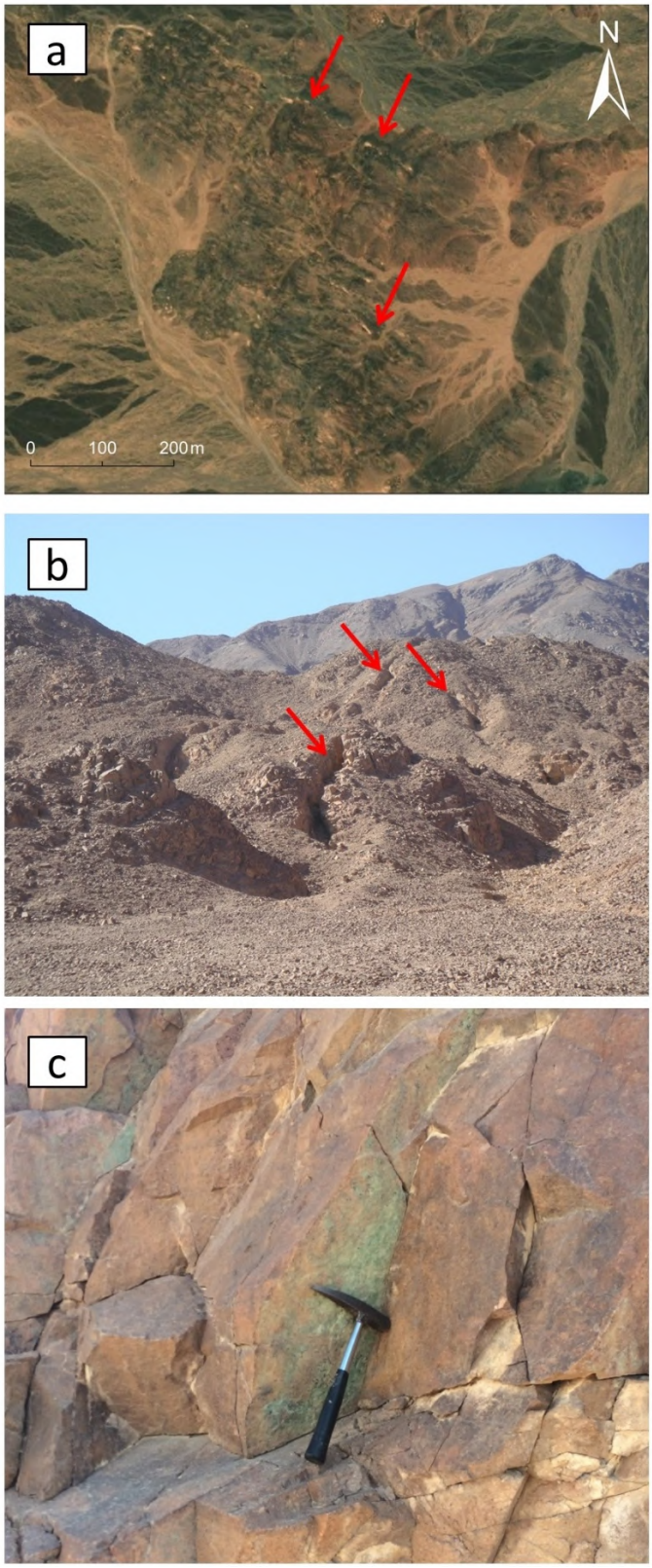

Figure 3. a) Satellite image of the GKZ prospect showing the alignment of ancient activities to the NW-SE direction within the granodiorite (marked by the red arrows). b) Well-developed shafts (excavated) in the granodiorite at the GKZ prospect (marked by the red arrows). c) Secondary copper minerals staining the joints in the granodiorite at the GKZ prospect.

Regarding the other prospect in this study, the GKZ is known for ancient mining activities in the vicinity of the west Wadi Dara prospect [27, 28, 39]. Ancient mining trenched in the GKZ prospect followed well-defined NW-trending structures (Figure 3a and b). The area comprises a thick volcano-sedimentary succession and is represented by intercalated Dokhan volcanics and Hammamat sediments [33, 34]. Remote sensing work that was confirmed by Field investigations (Figure5 and 6), revealed that the Neoproterozoic rocks in the prospect are dominated by granodiorite and quartz-feldspar porphyryand diorite. The present study considered the Au-Cu mineralizations of the ancient mining sites hosted by diorite, quartz-feldspar porphyry, and granodiorite.

Diorite represents the oldest rock type exposed in the GKZ area. The diorite covers a relatively vast area and occupies the southern part of the mapped area (Figure 6b). It occurs as low to moderate hills with gentle slopes. It has grayish green color and it is mesocratic. The diorite is equigranular and consists mainly of plagioclase and amphiboles. In some instances, the diorite exhibits some extents of heterogeneity in grain size (very coarse-to medium-grained) and in composition (gabbro to diorite). Only one variety of older granitoids in the GKZ area was distinguished, which is the granodiorite. The granodiorite is highly sheared and jointed. These fractures exhibit a well-developed conjugate system, which can be identified both on megascopic and microscopic scales. Boudinaged gold-bearing quartz veins (as thin as 10-15 cm), as well as secondary copper and iron minerals, fill into these fractures (Figure3c). In the hand-specimens, the granodiorite is light-colored and has a pinkish to reddish appearance due to predominance of feldspars. It is generally medium-grained and exhibits a porphyritic texture, with large white plagioclase phenocrysts. there is a huge amount of dumps surrounding the old excavations of the ancient workings in the prospect. Despite the presumably extensive metal extraction during the Arab times, the dumps still preserve valuable specimens with secondary Fe- and Cu-minerals dominated by Fe-oxyhydroxide and chrysocolla. Quartz-feldspar porphyry (dacite porphyry) is less predominant relative to the granodiorite in the northwestern part of the mapped area (Figure 6b). This porphyry is fine-grained, inequigranular and mostly leucocratic. It composed of plagioclase and quartz phenocrysts embedded in a reddish groundmass. The quartz-feldspar porphyry is intensively sheared in the same way to the adjacent granodiorite. Generally, the joint-dominated fractures are variably inclined and are occasionally vertical.

3. Dataset and Methodology

Satellite data used in this study originated from different multispectral spatial satellite data, which are frequently used for geological mapping, detection of alteration zones, and density of lineaments. Landsat-8 (LC08_L1TP_175041_20190117_20190131_01_T1) and Sentinel-2 (S2A_MSIL1C_20191018T081941_N0208_R121_T36RV_20191018T103632.SAFE) were downloaded from the United States Geological Survey (USGS) website (http://glovis.usgs.gov/). A scene of Landsat-8 image (path 175, row 041) including SGUM and GKZ prospect is used for this study. The output format of Landsat-8 is (GeoTIFF) with 1 quality assessment band image (GeoTIFF) and 1 metadata file (ASCII). All Landsat-8 and Sentinel-2 images are set in UTM /WGS84 datum and zone 36N.

Table 1. Band wavelengths for Landsat-8 OLI and Sentinel-2 MSI.

Landsat-8			Sentinel-2		
Band number	**Wavelength (nm)**	**Spatial resolution (m)**	**Band number**	**Wavelength (nm)**	**Spatial resolution (m)**
2	450-515	30	2	458-523	10
3	525-600	30	3	543-578	10
4	630-680	30	4	650-680	10
5	845-885	30	8	785-900	10
6	1560-1660	30	11	1565-1655	20
7	2100-2300	30	12	2100-2280	20

Procedures of this investigation rely on the integration between the optical satellite data (Landsat-8, Sentinel-2, and QuickBird) and GIS modeling. Flow sheet for the generation of the predictive models (PMs) is presented in Figure 4. In addition to pre-processing techniques (geometric correction and atmospheric correction), some image processing techniques such as minimum noise fraction, band math, band ratio, Principal Component Analysis (PCA) and

lineament analysis have been carried out to discriminate the different lithologies, to delineate the alteration zones and the ancient workings and to locate structural lineaments. Pre- and post-processing of different satellite data were carried out using the Environment for Visualizing Images (ENVI) version 5.3, PCI Geomatica, 2016, and the Arc GIS pro-2.8 software. Sentinel-2 and Landsats have the same geographic coordinate system and similar wavelengths (Table 1). Accordingly, this provide an excellent opportunity to combine these two types of data in order to obtain a higher accuracy in the results. All the available satellite images were fused with band 2 of Sentinel-2 using the Gram-Schmidt Pan-Sharpening method. Four data layers (thematic maps) have been generated from different sources of the satellite data. The thematic maps were utilized as inputs to generate the PMs for gold and copper mineralizations in the SGUM and GKZ prospects (i.e.). The input datasets involve updated geological maps (lithology layer), old pits/trenches buffer analysis, alteration zone maps, and lineament density maps. All the previous layers were prepared for the GIS-based PMs using knowledge-driven and weighting techniques. Gold-and-copper favorability maps were validated using well-documented data from previous works as well as the current field and petrographic studies.

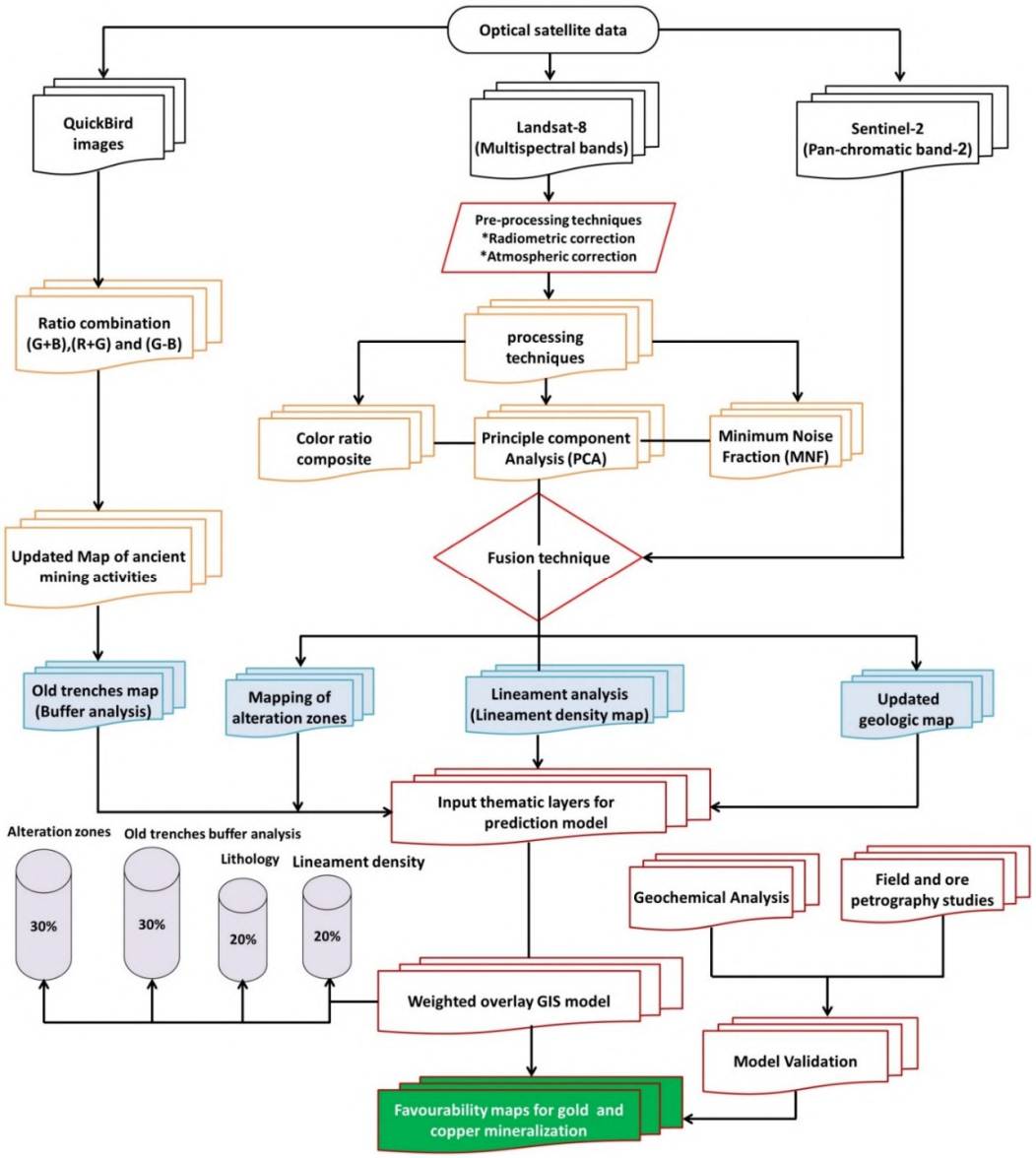

Figure 4. Flow chart of the methodology showing the various steps used to generate favorability/predictive maps (PM) for gold and copper mineralizations at the two investigated prospects in the NED of Egypt.

4. Results and Discussion

4.1. Preparation of thematic layers

The credibility of the PCA technique was approved by several studies, which considered the lithological discrimination and the hydrothermal alteration mapping [١, 10, 14, 40-43]. In the SGUM and GKZ prospects, the PCA was performed for the six bands of (visible, NIR, and SWIR) sub-systems of the Landsat-8 data. The PCA results of the eigenvalues (Table 2) indicate that the PC1 displays the highest variance amounting 97.1% of the total variances of the Landsat-8 data. PC1, 2, 3, and 4 together represent 99.7% of the total variance and spectral information content of the data. The rest bands represent the remaining 0.3% of the weight. Similar to the PCA, the MNF technique was used to compute the Landsat-8 visible, NIR, and SWIR. The first MNF contains the maximum variance and minimum noise and the last MNF contains the minimum variance and maximum noise. Detailed visual inspection of the first four PC was combined in red, green, and blue (RGB) and indicated that the false-color composite (FCC) image of PC2 (R), PC1 (G), and PC4 (B) represent the best color composite image for the lithological discrimination of the GKZ area in particular. MNF technique is applied to reduce data dimensionality and to remove noise from the spectral data [44]. The computed data indicate that the MNF color composite, MNF1(R), MNF3 (G), and MNF4 (B) is the best combination for the classification of the different rock units at the GKZ area. Integration of PCA and MNF results revealed a significant delineation and discrimination of the lithological contacts between the rock units. The results of PCA image show that the granodiorite has a rose image signature whereas quartz-diorite shows pink color (Figure 5a). The MNF successfully discriminated granodiorite, in distinct blue color, from the Dokhan volcanics, in light green color, and from diorite, in dark green color, (Figure 5b). These results were verified during field work, and correlated with some previous published maps for the investigated areas [30, 34, 35, 37]. Finally, field data together with the above-mentioned results were used to generate new geological maps for the SGUM and GKZ prospects (Figures 6a and b).

Table 2. Eigenvector matrix and Eigenvalues percentage of PCA results of Landsat-8 data at the area of study.

Eigenvector	Band 2	Band 3	Band 4	Band 5	Band 6	Band 7	Eigenvalue%
PC1	-0.161159	-0.257743	-0.373829	-0.469988	-0.558179	-0.485176	97.11
PC2	0.215134	0.295052	0.434612	0.475252	-0.484795	-0.465707	2.34
PC3	-0.280481	-0.368511	-0.068957	0.357771	0.527799	-0.611722	0.3
PC4	0.298489	0.465107	0.178515	-0.567223	0.414552	-0.411238	0.15
PC5	-0.577515	0.170221	0.736241	-0.297424	-0.053295	0.064413	0.02
PC6	0.653036	-0.682211	0.304453	-0.12265	0.012035	0.015882	0.01

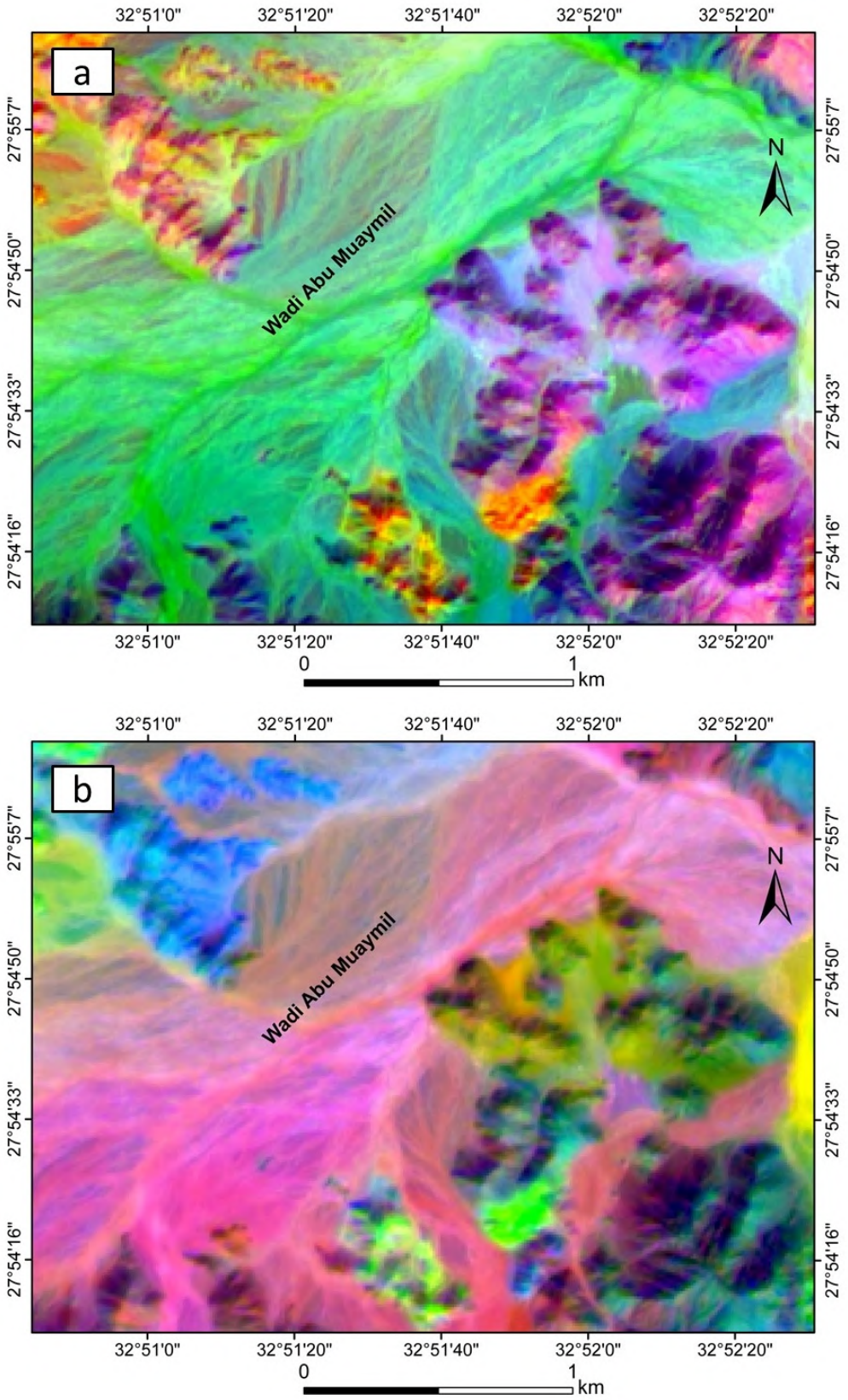

Figure 5. a) Landsat-8 false color composite (FCC) image PC2, PC1, PC4 in RGB for the GKZ prospect. b) Landsat-8 MNF false color composite (FCC) image MNF1, MNF3, and MNF4 in RGB for the GKZ prospect.

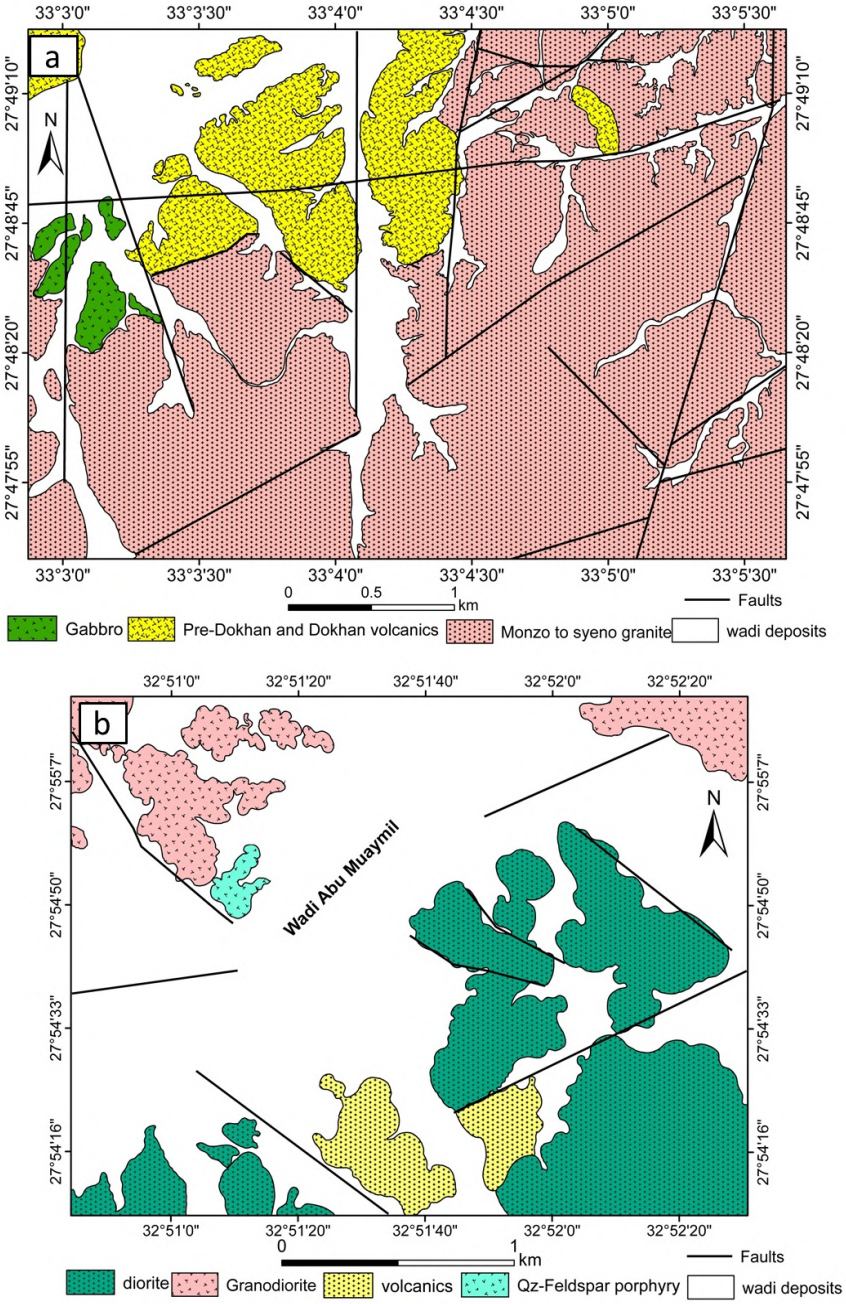

Figure 6. a) Geological map of SGUM prospect modified after [30, 31]. b) Geological map of the GKZ prospect modified after [37].

Extraction of geological linear features such as faults, joints, and fracture lines can be effectively achieved using satellite images [16, 17, 22, 45-47]. The lineaments were automatically detected using the model line of PCI Geomatica 2016. The default parameters of the software were adjusted as follows: Filter radius (pixels) = 10, edge gradient threshold = 30, curve length threshold (pixels) = 10, line fitting error threshold = 3, angular difference threshold (degrees) = 3, and linkage distance threshold (pixels) = 20. The high spatial resolution bands of the Sentinel-2 and principle component bands were visually tested, and the results revealed that the PC1 is the optimal band for the lineament extraction. PC1 is fused to obtain high-quality lineament maps. The extracted lineaments were visually inspected to delete and to edit incorrect lineaments (Figures 7a and b). Rose

diagrams show that the orientation of the extracted lineaments (Figure 8c) in the SGUM prospect mostly follow the NE-SW trend, whereas the lineaments in the GKZ prospect area show various trends. The lineament density analysis was calculated using the sum of the length of the lineament per unit area, and then the extracted lineaments were contoured to obtain a lineament density map using the line density tool in the ArcGIS software. Areas characterized by the highest density of lineaments are represented by red color whereas green color represents zones of low density (Figures 7c and d).

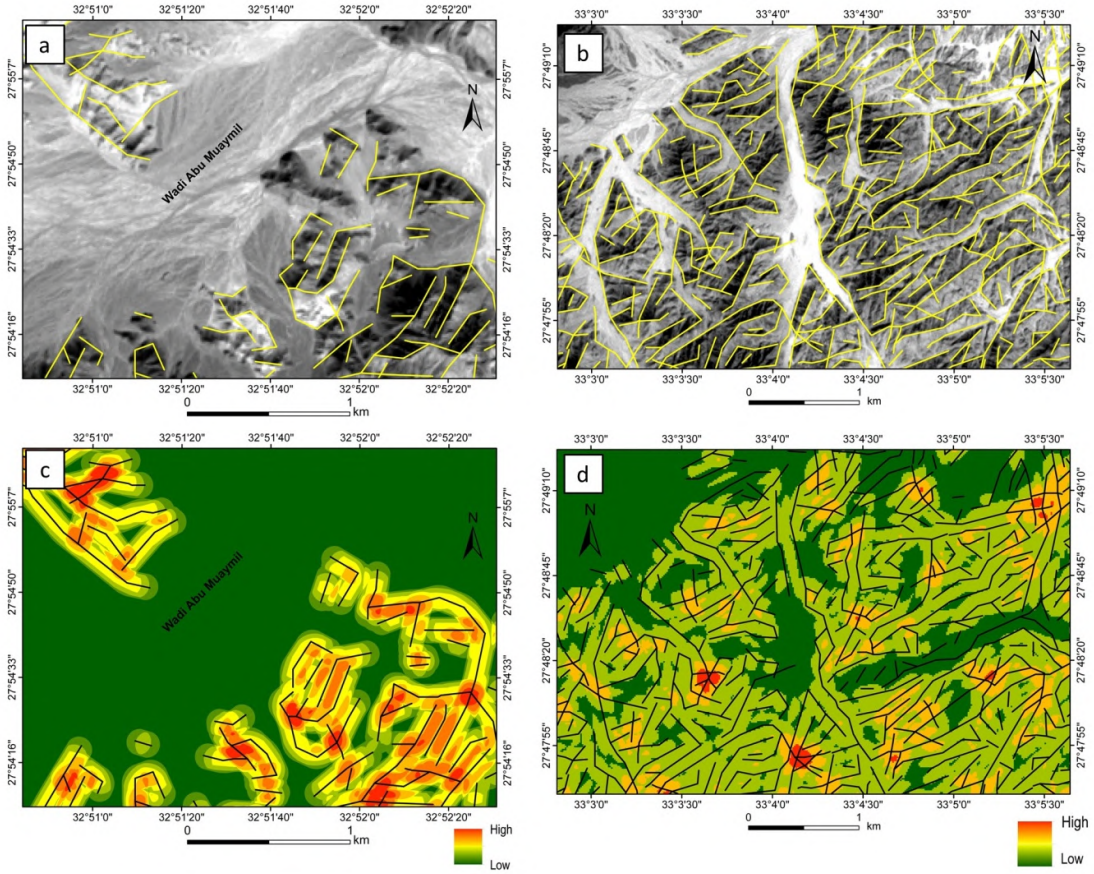

Figure 7. a) Distribution of major lineaments over PCA1 for the GKZ prospect. b) Distribution of major lineaments over PCA1 for the SGUM prospect. c) Density map of the extracted lineaments for the GKZ prospect using the line density tool. d) Density map of the extracted lineaments for the SGUM prospect using the line density tool.

As mentioned earlier, The GKZ and SGUM prospects are characterized by ancient mining activities for copper and gold mineralizations [28, 29]. Walls of old mining activities are stained by secondary green copper (Figure 3c) and reddish-to-black iron materials (Figure 2b). QuickBird ratio combinations (G+B), (R+G,) and (G-B) for RGB, were utilized to delineate the ancient mining activities (Figures 8a and b based on detailed field observations, the walls of old trenches indicate intensive deformation and alteration of host rocks. The old trenches layers are buffered to 20m wide bands in all directions (Figures 8a and b). This distance was found to be suitable for alteration zones that host gold and copper mineralizations. The rose diagrams indicate that the ancient activities in the GKZ prospect are aligned mostly in the NW-SE direction (Figure 8c). Old trenches at the SGUM prospect show heterogeneous direction with the ascendancy of the lineaments following the NE-SW and NW-SE trends (Figure 8c).

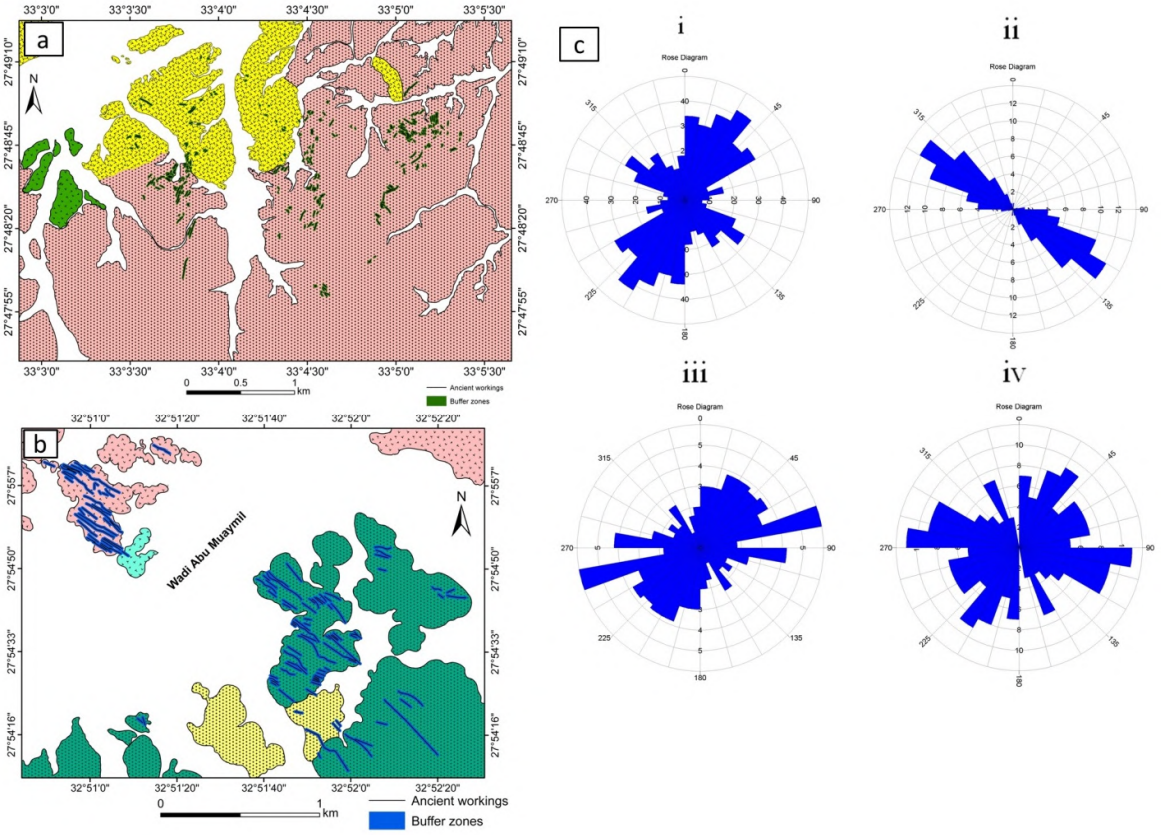

Figure 8. a) Buffer analysis of the extracted old workings (mines) at the SGUM prospect. b) Buffer analysis of the extracted old trenches at the GKZ prospect. c) Rose diagrams showing the dominant directions of ancient pits at the SGUM prospect (i), and the GKZ prospect (ii). In (iii) and (iv), the main directions of lineaments at the SGUM and GKZ prospects, respectively, are shown.

Mapping and delineation of the alteration zones are essential targets of gold and copper exploration. The operation of band ratio is likely effective in mapping and detecting alteration zones associated with gold mineralization [8, 1١, 15, 44, 48, 49]. Sericitization, silicification, chloritization, and kaolinitization are the most common wall rock alteration at SGUM and GKZ prospects [36, 37]. In terms of the mineralization style, the SGUM prospect likely represents a porphyry copper system [30] or an iron oxide-rich Cu-Au porphyry-style system, i.e. an IOCG ore [3١, 36]. The iron oxide minerals are hematite (specularite), limonite, magnetite, and goethite. The present study utilized the Landsat-8 color ratio composite (6/5 * 4/5, 6/7, and 6/2) for the RGB, respectively (Figure 10a). These band ratios were tested and selected based on the spectral characteristics of the host rocks and their associated alteration zones. Figure 9 shows the spectral reflectance and absorption of some hydrothermally altered minerals at GKZ and SGUM prospects. The Landsat-8 6/5 ratio was used for detecting ferrous (Fe^{2+}) minerals such as hematite [50], and the 6/7 ratio is for detecting altered rocks containing clay and other minerals that contain a hydroxyl group (OH^-) [4, 43]. The band ratio (6/5 * 4/5) was used for detecting Fe-bearing minerals [51]. The utilized ratio composite (6/5 * 4/5, 6/7, and 6/2) successfully mapped and discriminated altered rocks from the fresh parental rocks [51]. The altered rocks have a distinctive orange color in both the SGUM and GKZ prospect (Figures 10a and b). The analyzed images were tested by field observations to confirm the alteration zones. The coincidence of these types of mineralization with the alterations zones suggests a high degree of gold and copper potentialities.

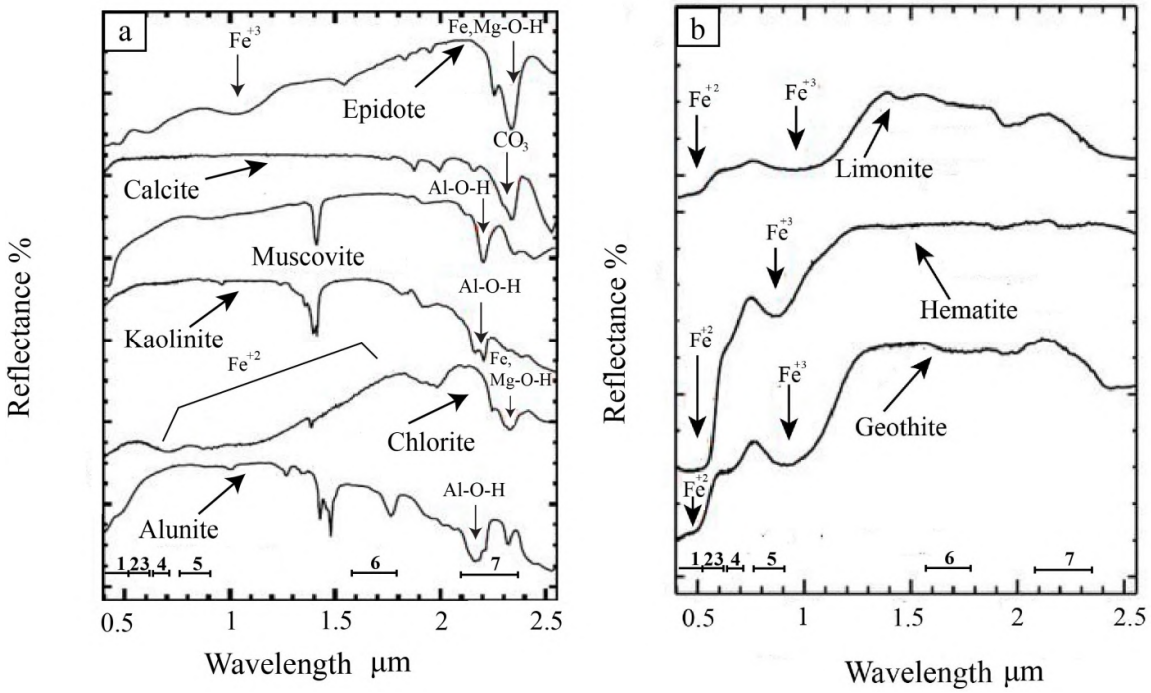

Figure 9. a) Laboratory spectral curves for muscovite, chlorite, kaolinite, alunite, calcite, and epidote. b) Laboratory spectral curves for limonite, hematite, and goethite [52].

4.2. Application of GIS knowledge-driven method

The spatial relationship of the input dataset with the gold and copper occurrences is quantified using the weight of evidence and knowledge-driven methods. The approach of predictive models (PMs) is applied here to integrate the different datasets into gold and copper prospection maps for any future work in the two investigated prospects, as well as similar areas in the Eastern Desert of Egypt and in neighboring countries. The PMs were constructed by overlaying cumulative weight assigned to the four thematic layers (maps of lithology, lineament density, old trench density, alteration zones) by applying the weighted overlay method in the spatial analysis tool in the ArcGIS pro 2.8. Table 3 summarizes the weight and score values for the obtained thematic maps and their contribution to the occurrences of gold and copper mineralizations. The score for each dataset is determined based on the favorability degree of gold and copper occurrences at the SGUM and GKZ prospects. The greater the spatial association to mineralization, the larger the scores of the dataset. Field observations and analyses obtained from the different remote sensing data revealed that the old excavations and alteration zones are hosted in the diorite, granodiorite, and quartz-feldspar porphyry rocks at the GKZ prospect, while in the SGUM prospect, they are hosted in the Dokhan volcanics and the monzogranite. There is no evidence of any ancient or contemporaneous mining activities neither in the gabbro cropping out at the SGUM prospect nor in the Dokhan volcanics at the GKZ prospect. Much of the mineralized zones were excavated in antiquity from shallow depths ranging from 3 to 7 m, and therefore these zones most likely extend to deeper levels in the subsurface and possibly hit a primary or hypogene ore. These zones are rich in secondary copper minerals in addition to specularite and barite (Figure 2b), which appear as gossans-like bodies. Among the four input layers, the highest scores were assigned to the buffer zones of ancient workings (30%) and similarly to the alteration zone maps (30%). Moderately high weights were assigned to the lithology maps and to lineament density maps (20%).

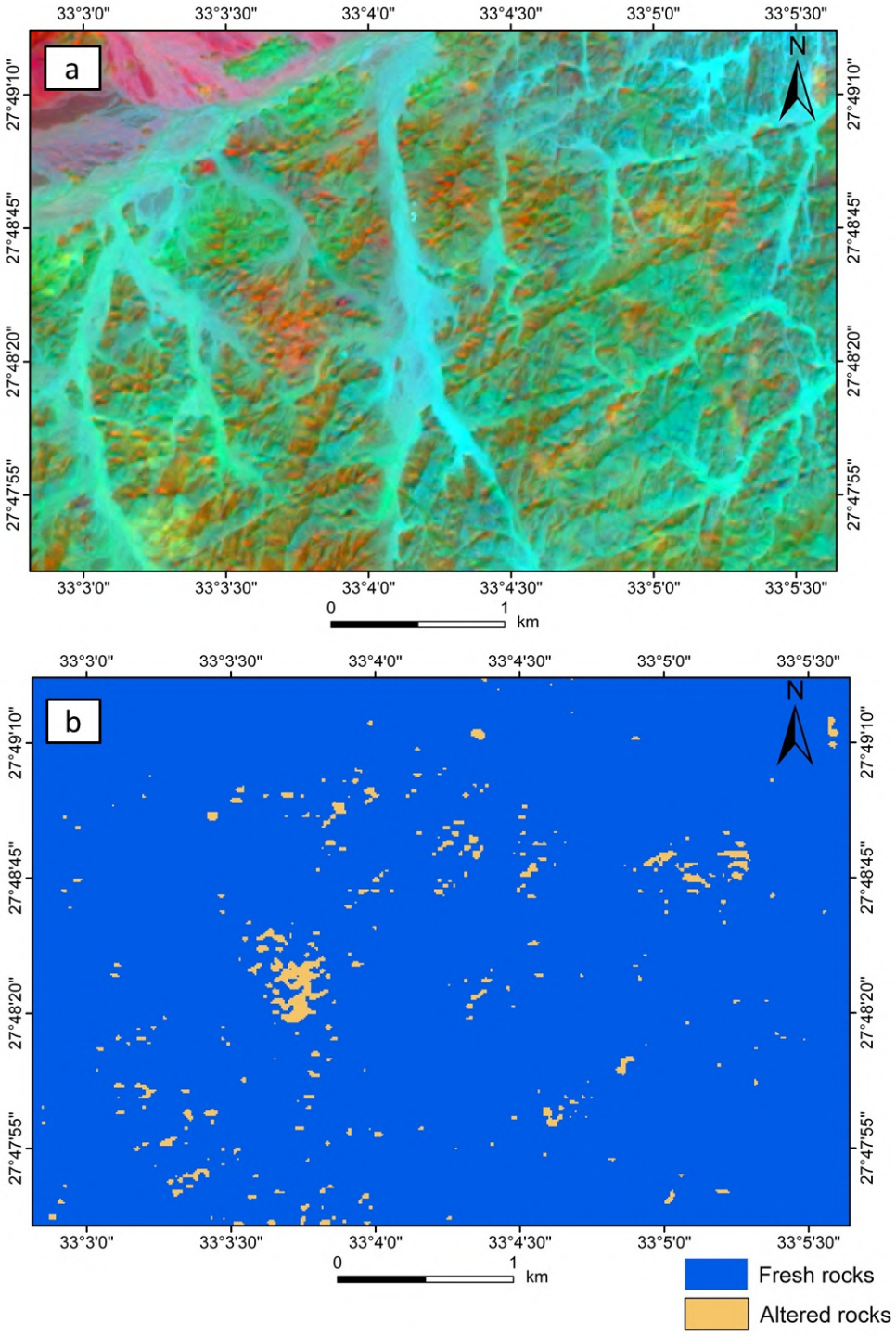

Figure 10. a) Landsat-8 band ratios composite image (6/5 * 4/5, 6/7, and 6/2) in RGB for the SGUM prospect showing altered rocks as orange color spots. b) Distribution of altered rocks (orange color) extracted from the band ratio image for the SGUM prospect.

The application of weighted overlays mainly concerns the raster format. The lithology layers were rasterized and then reclassified into three classes for the SGUM prospect and four classes for the GKZ prospects, in which each rock unit has a distinctive weight (Table 3). Alteration zone maps were reclassified into two classes, one for altered zones and the other for non-altered zones or fresh rocks (Figures 10a and b). Density maps for the lineament analysis were reclassified to integer

numbers ranging from 1 to 5. Classes with higher potential for gold and copper mineralizations were assigned to have 5, whereas classes with low mineralization potential were assigned to have 1. Classes with moderate contribution were assigned to have 3. The lineament density maps were assigned from 1 to 5 on ascending order of increasing density. The extracted maps from buffer analysis were weighted internally, whereas the buffered zones (highest favorable) were assigned to have 5 whereas the other sites have 1. Then, each class within the thematic layers was weighted from 1 to 5 based on its contribution to the occurrences of gold and copper mineralizations. Diorite, granodiorite, and quartz-feldspar porphyry rocks at the GKZ prospect, in addition to Dokhan volcanics and granitic rocks of the SGUM prospect, were assigned to have high potentiality ranks. The other rock units were assigned to have lower potentiality ranks. The non-altered zones were assigned to low rank and the altered zones were assigned to high rank. The results of PMs for the Au-Cu mineralizations at the SGUM and GKZ prospects are shown in Figures 11a and b. Two main types of gold and copper deposits were documented at the SGUM prospect. The first one is a porphyry copper system with a defining five alteration zones namely; potassic, phyllic, phyllic-argillic, sodic, and propylitic zones (Figure1a) [30, 36]. The second is iron oxide-rich Cu-Au porphyry-style systems (IOCG) [31, 36]. The prospective sites at SGUM are associated mainly with potassic, sericite-chlorite, and sodic zones (Figure 11a). The GKZ prospect has no previous remote sensing studies concerning mapping alteration zones. Detailed field and microscopic investigations revealed that hydrothermal IOCG deposits are the most dominant phase at SGUM and GKZ prospects. The suggested models in this study present several new prospective sites for IOCG exploration at SGUM and GKZ prospects (Figures 1a and b).

Table 3. Weight and score for the different thematic maps by their potentialities for gold and copper mineralizations.

Parameter	Class		Weight	Score	Au and Cu mineralization potentiality				
					Very high	High	Moderate	Low	Very low
Lineament density maps	Class 5 (high)		5	20%					
	Class 4		4						
	Class 3		3						
	Class 2		2						
	Class 1 (low)		1						
Ancient workings buffer analysis	Buffered zones		5	30%					
	Non-buffered zones		1						
	SGUM area	**GKZ area**							
	Granodiorite	Monzogranite	5	20%					
	Dokhan volcanics	Quartz feldspar porphyry	5						
		Diorite	5						
	Gabbro	Dokhan volcanics	2						
Alteration zone maps	Altered rocks		5	30%					
	Non-altered rocks		2						

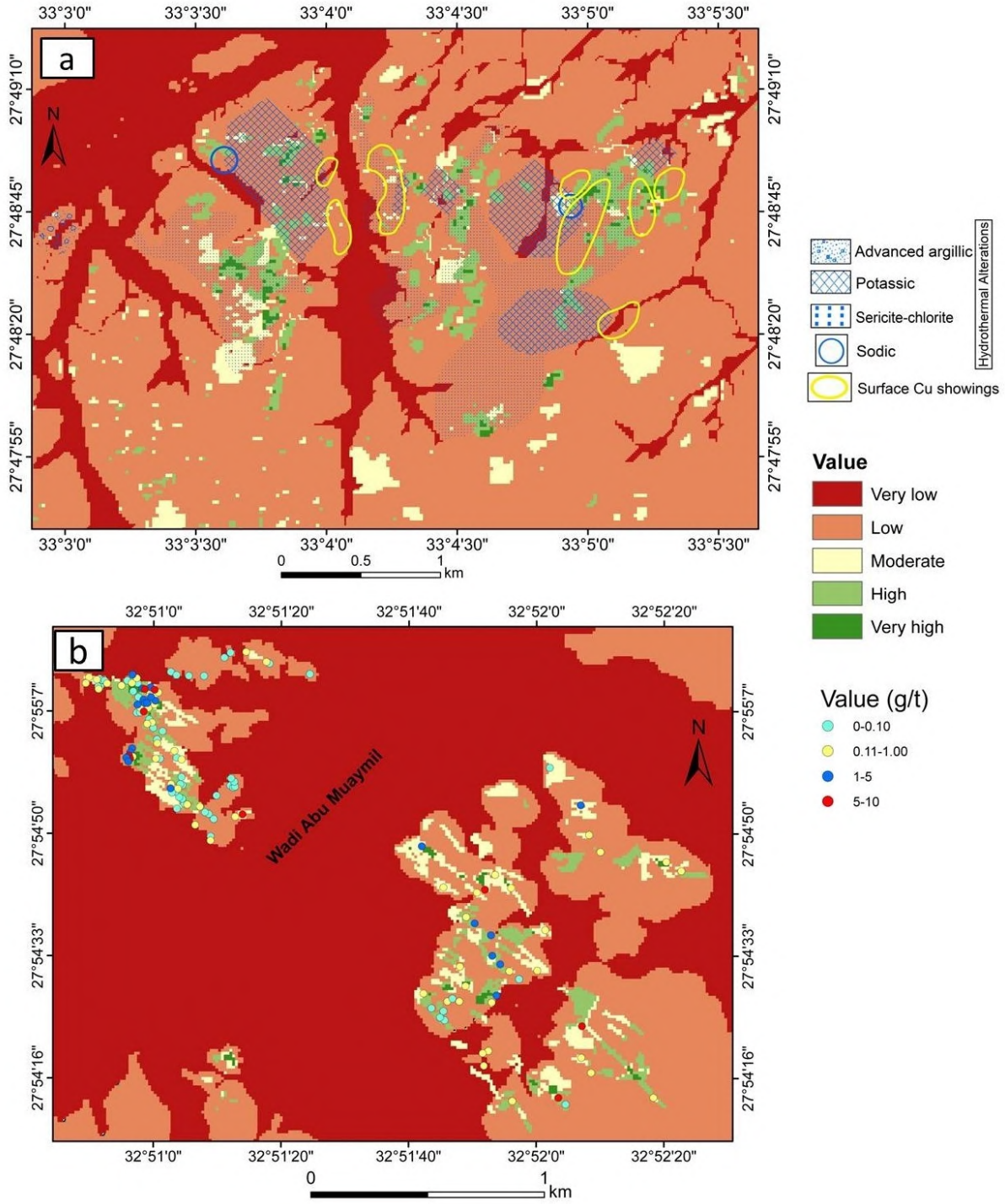

Figure 11. a) Favorability/predictive map (PM) for Au and Cu mineralizations over the SGUM prospect. b) PM for Au and Cu mineralizations over the GKZ prospect. Overlies of the alteration zones, Au contents, and Cu anomalies were obtained from [30, 36, 53].

5. Validation of Suggested Model

Validation of the obtained gold and copper PMs is important to test the reliability and precision/accuracy of the results. The PMs for gold and copper mineralizations at the SGUM and GKZ prospects were validated using the known gold and copper occurrences from previous works [30, 31, 36]. For further validation, the results are compared with [31, 53]. The concentrations of gold and

copper in ppm were obtained mainly from analytical analysis of more than 130 samples that have been detected by the Egyptian Mineral Resources Authority [53] using the fire assay technique for the analysis of gold. The results show that the potential areas obtained from the PMs (Figure 11) are correlated with areas (overlies) of high gold and copper anomalies. This confirms the validation of the proposed PMs. Also, this was supported by field data on the mineralized zones in the two prospects. Contribution of this study to the NED is in harmony with some recent research on the localization of gold deposits in the Eastern Desert of Egypt [54]. Previous research was able to combine imagery data from Landsats and air-borne magnetic surveys to confirm and delineate gold-rich shear zones and alteration zones in sites known for gold mineralization in the CED and SED. Therefore, integration of the present findings with those from [54-56] may represent a very useful model for predicting areas with high gold potentialities in the Eastern Desert. and other arid terrains.

Additionally, some polished and polished-thin sections were prepared from the newly prospective alteration zones to define opaque minerals of the potential mineralized zones. The microscopic investigations revealed that the mineralized zones at SGUM and GKZ prospects consist of iron oxide and sulfide minerals. The hydrothermal mineralization is confined to the shear zones. The shear zones are characterized by the presence of copper and iron minerals. The alteration products are related mainly to post-magmatic hydrothermal solutions that were responsible for the development or mobilization of iron, copper, and gold. The iron oxide minerals are hematite (specularite), magnetite, limonite and goethite. Sulfide minerals are represented by pyrite and chalcopyrite. In hand specimens, the iron oxides (magnetite and specularite) occur as coarse-grained crystals filling the fractures and crystallized in between quartz crystals. Specular hematite is present in a significant amount in both SGUM and GKZ prospects. Specularite is medium-grained occurring in the form of flaky or fibrous crystals that crosscut each other. Other specular crystals of hematite are radiating from a common center forming a fan-shape. They are randomly oriented. However, they are sometimes showing certain alignments parallel to each other (Figure 12a). Magnetite occurs as coarse, euhedral to subhedral, tabular, irregular, and long prismatic crystals. Magnetite is highly martitized along the cleavage and along the peripheries of the crystals (Figure 12b). Pyrite is mostly oxidized and occurs as medium-grained in size and equant in shape (Figure 12c). Chalcopyrite shows either slight alteration or complete replacement to goethite. Chalcopyrite is partially altered to covellite along its peripheries. Goethite occurs as large pseudomorphic crystals after pyrite and chalcopyrite and it exhibits perfect colloform texture (Figure 12d). Gold occurs either as randomly tiny speaks in quartz crystals or as aligned speaks filling microfractures (Figure 12c).

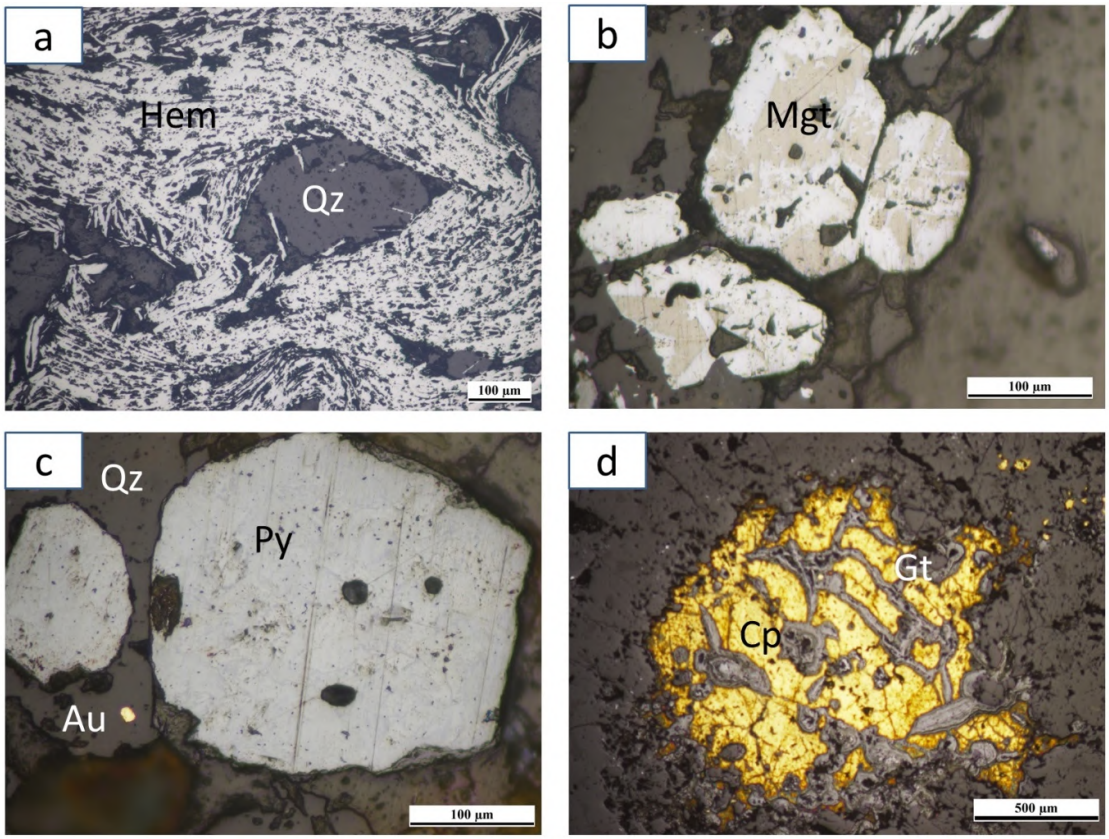

Figure 12. Ore minerals in the mineralized alteration zones at SGUM and GKZ prospects. All photomicrographs in reflected light. a) Sheared specularite (hematite) (Hem) at SGUM prospect. b) Highly martitized magnetite at SGUM prospect. c) Oxidized pyrite (Py) and possible gold speak (Au) at SGUM prospect. d) Partial replacement of chalcopyrite (cp) by goethite (Gt) at GKZ prospect.

6. Conclusions

Utilization of remote sensing data and GIS combined with the field observations, petrography, geochemical analyses, and historical data seem to be effective for highlighting areas with high mineralization potentialities. The findings in this study are summarized as follows:

1) Combining results from false color composite images of PC2 (R), PC1 (G), and PC3 (B) in addition to MNF1(R), MNF2 (G), and MNF3 (B) have successfully classified the host rocks in SGUM and GKZ gold-copper prospects.

2) Lineament density maps were generated after extraction of lineaments using line module over PCA images. 3) Buffer analysis maps were generated after extracting ancient workings sites using ratio combination (G+B), (R+G) and (G-B) for RGB of QuickBird imageries.

4) Landsat-8 band ratios imagery (6/5*4/5, 6/7 and 6/2) in RGB was successfully delineated alteration zones that host gold and copper mineralizations.

5) The scores 30%, 30%, 20%, and 20% were assigned to alteration zone maps, old trenches buffer analysis, lithology map and lineament density maps, respectively.

6) Results of the suggested PMs were classified into five zones: very low, low, moderate, high, and very high corresponding to variable potentials for mineralization. Various new potential sites for gold and copper occurrences at SGUM and GKZ prospects were suggested.

7) Field, geochemical, and petrographic studies to SGUM and GKZ prospects validated the suggested model.

8) The obtained PMs would provide a useful insight for further exploration in the future in areas similar to the GKZ and SGUM prospects elsewhere in the ANS and other world examples of Neoproterozoic shield terrains. Therefore, we believe that the suggested PMs can be valid for different kinds of economic potentialities, not only for metallic ores viz. Au and Cu, but for non-metallic ores as well.

Acknowledgments

The paper is extracted from the MSc Thesis by the first author. The authors are indebted to the logistic field and laboratory support from the Faculty of Science, Cairo University. Sincere help from Ahmed Abd El-Dayiem during the fieldwork is greatly acknowledged.

Limitations

The prediction model presented in this study could be applicable only in arid and semi-arid regions.

References

[1]. Zhang, X., Pazner, M., & Duke, N. (2007). Lihologic and mineral information extraction for gold exploration using ASTER data in the south Chocolate Mountains (California). *Journal of Photogrammetry and Remote Sensing, 62*, 271-282.

[2]. Madani, A., & Harbi, H. (2012). Spectroscopy of the mineralized tonalite–diorite intrusions, Bulghah gold mine area, Saudi Arabia: effects of opaques and alteration products on FieldSpec data. *Ore Geology Reviews, 44*, 148–157.

[3]. Han, T., & Nelson, J. (2015). Mapping hydrothermally altered rocks with Landsat 8 imagery: a case study in the KSM and Snowfield zones, northwestern British Columbia. In: Geological Fieldwork 2014, British Columbia Ministry of Energy and Mines. *British Columbia of Geological Survey Paper, 1*, 103–112.

[4]. Pour, A.B., & Hashim, M. (2015). Hydrothermal alteration mapping from Landsat-8 data, Sar Cheshmeh copper mining district, south-eastern Islamic Republic of Iran. *Journal of Taibah University for Science, 9*, 155-166.

[5]. Moradi, M., Basiri, S., Kananian, A., & Kabiri, K. (2015). Fuzzy logic modeling for hydrothermal gold mineralization mapping using geochemical, geological, ASTER imageries and other geo-data, a case study in Central Alborz, Iran. *Earth Science Informatics, 8* (1), 197-205.

[6]. Gahlan, H., & Ghrefat, H. (2018). Detection of gossan zones in arid regions using Landsat-8 OLI data: implication for mineral exploration in the Eastern Arabian Shield, Saudi Arabia. *Natural Resources Research, 27* (1), 109-124.

[7]. Safari, M., Maghsoudi, A., & Pour, A.B. (2018). Application of Landsat-8 and ASTER satellite remote sensing data for porphyry copper exploration: a case study from Shahr-e- Babak, Kerman, south of Iran. *Geocarto International, 33*(11), 1186-1201.

[8]. Pour, A.B., Hashim, M., Park, Y., & Hong, J.K. (2018). Mapping alteration mineral zones and lithological units in Antarctic regions using spectral bands of ASTER remote sensing data. *Geocarto International, 33* (12), 1281-1306.

[9]. Sultan, M., Arvidson, R.E., & Sturchio, N.C. (1986). Mapping of serpentinites in the Eastern Desert of Egypt using Landsat thematic mapper data. *Geology, 14*, 995-999.

[10]. Madani, A. (2001). Geological studies and remote sensing applications on Wadi Natash volcanic, Eastern Desert, Egypt. *Ph.D. thesis, Faculty of Science, Cairo University*.

[11]. Madani, A. (2003). Evaluation of the Fusion of Landsat Thematic Mapper Imagery and Scanned Aerial Photograph for Mapping the Trachytic ring dykes, Wadi Natash area, South Eastern Desert, Egypt. *5th International Conference on Geology of the Middle East*, 509-517.

[12]. Ramadan, T.M. & Kontny, A. (2004). Mineralogical and structural characterization of alteration zones detected by orbital remote sensing at Shalatein District, SE Desert of Egypt. *Journal of African Earth Sciences, 40*, 89-99.

[13]. Gad, S., & Kusky, T. (2007). ASTER spectral rationing for lithological mapping in the Arabian–Nubian Shield, the Neoproterozoic Wadi Kid area, Sinai, Egypt. *Gondwana Research, 11* (3), 326-335.

[14]. Gabr, S.S., Ghulam, A., & Kusky, T. (2010). Detecting areas of high-potential gold mineralization using ASTER data. *Ore Geology Reviews, 38* (1-2), 59-69.

[15]. Madani, A., & Emam, A.A. (2011). SWIR ASTER band ratios for lithological mapping and mineral exploration: a case study from El Hudi area, southeastern desert, Egypt. *Arabian Journal of Geosciences, 4*(1), 45-52.

[16]. Amer, R., Kusky, T., & El Mezayen, A. (2012). Remote sensing detection of gold-related alteration zones in Um Rus area, Central Eastern Desert of Egypt. *Advances in Space Research, 49*(1), 121-134.

[17]. Abou El-Magd, I., Mohy, H., & Basta, F. (2015). Application of remote sensing for gold exploration in the Fawakhir area, Central Eastern Desert of Egypt. *Arabian Journal of Geosciences, 8*(6), 3523–3536.

[18]. Salem, S.M., El Sharkawi, M.A., El-Alfy, M.Z., & Ahmed, S.E. (2018). The use of ASTER data and geochemical analyses for the exploration of gold in the Samut area, South Eastern Desert of Egypt. *Arabian Journal of Geosciences, 11*, 541.

[19]. Abu El-Leil, I., Soliman, N.M.A., Bekiet, M. H., & Elhebiry, M.S. (2019). Enhancing multispectral remote sensing data interpretation for historical gold mines in Egypt: a case study from Madari gold mine. *Arabian Journal of Geoscience,12*(1),1-10.

[20]. Nykanen, V., Groves, D.I., Ojala, V.J., Eilu, P., & Gardoll, S.J. (2008). Reconnaissance-scale conceptual fuzzy-logic prospectivity modeling for iron oxide copper-Gold deposits in the northern Fennoscandian shield, Finland. *Australian Journal of Earth Sciences, 55*(1), 25-38.

[21]. Madani, A. (2011). Knowledge-driven GIS modeling technique for gold exploration, Bulghah gold mine area, Saudi Arabia. Egypt. *Journal of Remote Sensing and Space Sciences, 14*(2), 91-97.

[22]. Magalhães, L.A. & Souza Filho, C.R. (2012). Targeting of gold deposits in Amazonian exploration frontiers using knowledge-and data-driven spatial modeling of geophysical, geochemical, and geological data. *Surveys in Geophysics, 33*(2), 211-241.

[23]. Lusty, P.A.J., Scheib, C., Gunn, A.G., & Walker, A.S.D. (2012). Reconnaissance-scale prospective analysis for gold mineralization in the Southern Uplands-Down-Longford Terrane, Northern Ireland. *Natural Resources Research, 21*(3), 359-382.

[24]. Harris, J. R., Grunsky, E., Behnia, P., & Corrigan, D. (2015). Data-and knowledge-driven mineral prospectivity maps for Canada's north. *Ore Geology Reviews, 71*, 788-803.

[25]. Yousefi, M., Carranza, E. J.M., Kreuzer, O.P., Nykänen, V., Hronsky, J. M., & Mihalasky, M.J. (2021). Data analysis methods for prospectivity modelling as applied to mineral exploration targeting: State-of-the-art and outlook. *Journal of Geochemical Exploration, 229*, 106839.

[26]. Botros, N.S. (2015). Gold in Egypt does the future get worse or better? *Ore Geology Review, 67*, 189-207.

[27]. Tawab, M.A., Castel, G., Pouit, G., & Ballet, P. (1990). Archéo-géologie des ancienne mines de cuivre et d'or des régions El-Urf/Mongul-Sud et Dara Ouest. *Bulletin De L'institut Français D'Archéologie Orientale, 90*, 359-364.

[28]. Klemm, D., Klemm, R., & Murr, A. (2001). Gold of the Pharaohs–6000 years of gold mining in Egypt and Nubia. *Journal of African Earth Sciences, 33*, 643-659.

[29]. Osman, A. (1994). Native Gold Mineralization Associated with Iron Oxides, Mongul Area, northern Eastern Desert, Egypt. Middle East Research Center. *Ain Shams University, Earth Science Series*,74-87.

[30]. Botros, N., & Wetait, M. (1997). Possible porphyry copper mineralization in south Um Monqul, Eastern Desert, Egypt. *Egyptian Journal of Geology, 41*(1),175-196.

[31]. Fletcher, R.J. (2009). SMW Gold Limited NI 43-101 Technical Report on the Um Balad/ ElUrf Exploration Concession Area in Egypt (*Behre Dolbear Project Number J09-107*).

[32]. Breitkreuz, C., Eliwa, H., Khalaf, I., El Gameel, K., Bühler, B., & Sergeev, S. (2010). Neoproterozoic SHRIMP U–Pb zircon ages of silica-rich dokhan volcanics in the north Eastern Desert, Egypt. *Precambrian Research, 182*(3),163-174.

[33]. Eliwa, H., Breitkreuz, C., Murata, M., Khalaf, I., Bühler, B., Itaya, T., Takahashi, T., Hirahara, Y., Miyazaki, T., & Kimura, J. (2014). SIMS zircon U–Pb and mica K–Ar geochronology, and Sr–Nd isotope geochemistry of Neoproterozoic granitoids and their bearing on the evolution of the north Eastern Desert, Egypt. *Gondwana Research, 25*(4), 1570-1598.

[34]. Azzaz, S.A., Kharbish, S., & El-Alfy, H.M. (2015). Geological and geochemical investigations on Hammamat molasse sediments, G. Kharaza, Eastern Desert, Egypt. *Acta Universitatis Matthiae Belii, Seria Environmental Manazerstov, 2*, 7-28.

[35]. Abd El-Rahman, Y., Seifert, T., Gutzmer, J., Said, A., Hofmann, M., G¨artner, A., & Linnemann, U. (2017). The South Um Mongol Cu-Mo-Au prospect in the Eastern Desert of Egypt: from a mid-Cryogenian continental arc to Ediacaran post-collisional appetite-high Ba-Sr monzogranite. *Ore Geology Reviews, 80*, 250-266.

[36]. Abd El-Rahman, Y., Seifert, T., & Said, A. (2018). The South Um Mongol Cu-Mo-Au prospect in the northern Eastern Desert of Egypt: Tonian porphyry-style mineralization with an Ediacaran hydrothermal iron oxide overprint. *Ore Geology Reviews, 99*, 217-234.

[37]. El-Desoky, H.M. & Hafez, H.M. (2018). Petrology, Geochemistry, and Mineralogy of the Hydrothermally Altered Rock Units at Wadi Dara. north Eastern Desert, Egypt. *Annals of the Geological Survey of Egypt*, 103-140.

[38]. Kochine, G. G., & Bassuni, F. A. (1968) Mineral resources of the U.A.R.: Part I. Metallic minerals: Internal Report, *Geological Survey of Egypt*, 305-436.

[39]. El-Wardany, R., & Jiao, J. (2023). Perspective Chapter: History and Classification of Gold Mineralization in Egypt. In: M.T. Aide, Rare Earth Elements- Emerging Advances, Technology Utilization, and Resource Procurement, IntechOpen, Chapter 3, *https://doi.org/10.5772/intechopen.110042.*

[40]. Ferrier, G., White, K., Griffiths, G., & Bryant, R. (2002). The mapping of hydrothermal alteration zones on the island of Lesvos, Greece using an integrated remote sensing dataset. *International Journal of Remote Sensing, 23*(2), 341-356.

[41]. Crosta, A.P., Souza Filho, C.R., Azevedo, F., & Bro- die, C. (2003). Targeting key alteration minerals in epithermal deposits in Patagonia, Argentina, using ASTER imagery and principal component analysis. *International Journal of Remote Sensing, 24*, 4233-4240.

[41]. Liu, L., Zhou, J., Jiang, D., Zhuang, D., Mansaray, L. R., & Zhang, B. (2013). Targeting mineral resources

with remote sensing and field data in the Xiemisitai area, West Junggar, Xinjiang, China. *Remote sensing, 5*(7), 3156-3171.

[43]. Ali, A. S., & Pour, A. B. (2014). Lithological mapping and hydrothermal alteration using Landsat-8 data: a case study in ariab mining district, red sea hills, Sudan. *International Journal of Basic and Applied Sciences, 3*(3) 199.

[44]. Pour, A., & Hashim, M. (2011). Identification of hydrothermal alteration minerals for exploring porphyry copper deposit using ASTER data, SE Iran. *Journal of Asian Earth Sciences, 42*, 1309-1323.

[45]. Baumgartner, A., Ateger, C., Mayer, H., Eckstein, W., & Ebner, H. (1999). Automatic road extraction based on multi-scale, grouping, and context. *Photogrammetric Engineering and Remote Sensing, 65*, 777–785.

[46]. Madani, A. (2002). Selection of the optimum Landsat TM bands for lineament extraction, wadi Natash area, South Eastern Desert, Egypt. *Asian Journal of Geoinformatics, 3*, 71-76.

[47]. Arnous, M.O., ElMowafy, A.A., Azzaz, S.A., Omar, A.E., & Abdel Hafeez, W.M. (2021). Exploration radioactive mineralization using mappable data integration approach: an example from Wadi Dahab area, Southeastern Sinai, Egypt. *Arabian Journal of Geosciences, 14*,1-23.

[48]. Gabr, S.S., Sadek, M.F., & Hassan, S.M. (2015). Prospecting for new gold-bearing alteration zones in the El-Hoteib area, South Eastern Desert, Egypt, using remote sensing data analysis. *Ore Geology Reviews, 71*, 1–13.

[49]. Salem, S.M., El Sharkawi, M.A., El-Alfy, M.Z., Soliman, N.M., & Ahmed, S.E. (2016). Exploration of gold occurrences in alteration zones at Dungash district, Southeastern Desert of Egypt using ASTER data and geochemical analyses. *Journal of African Earth Sciences, 117*, 389-400.

[50]. Gupta, R.P. (2003). Remote sensing geology, *Springer, Heidelberg,* 438.

[51]. Fotze, Q.M.A., Lordon, A.E.D., Penaye, J., Sep, J.P., & Fru, M.I.N. (2019). Mapping hydrothermal alteration targets from Landsat 8 OLI/TIRS and magnetic data using digital image processing techniques in Garoua, north Cameroon. *Geoscience, 7*(1), 28-41.

[52]. Clark, R.N., Swayze, G.A., Wise, R., Livo, E., Hoefen, T., Kokaly, R., & Sutley, S.J. (2007). USGS digital spectral library splib06a: U.S. Geological Survey, Digital Data Series 231. *http://speclab.cr.usgs.gov/spectral-lib.html.*

[53]. EMRA (2013). Geological and geochemical Exploration of gold and copper deposits in basement rocks at Wadi Dara and in sedimentary rocks at Wadi Araba, north Eastern Desert, Egypt. *Internal Report (expedition No. G2-2013), Exploration Department, the Egyptian Mineral Resources Authority*, 124.

[54]. Gabr, S.S., Diab, H., Abdel Fattah, T.A., Sadek, M.F., Khalil, I.K., & Youssef, M.A.S. (2022). Aeromagnetic and Landsat-8 data interpretation for structural and hydrothermal alteration mapping along the Central and Southern Eastern Desert boundary, Egypt. *The Egyptian Journal of Remote Sensing and Space Science, 25*(1), 11-20.

[55]. Elkhateeb, S.O., & Eldosouky, A.M. (2016). Detection of Porphyry Intrusions Using Analytic Signal (AS), Euler Deconvolution, and Center for Exploration Targeting (CET) Technique Porphyry Analysis at Wadi Allaqi Area, South Eastern Desert, Egypt. *International Journal for Science and Engineering Research, 7*(6), 471-477.

[56]. Eldosouky, A.M., Sehsah, H., Elkhateeb, S.O., & Pour, A.B. (2020). Integrating aeromagnetic data and Landsat-8 imagery for detection of post-accretionary shear zones controlling hydrothermal alterations: The Allaqi-Heiani suture zone, South Eastern Desert, Egypt. *Advances in Space Research, 65*, 1008-1024.

یک مدل GIS پیش‌بینی‌کننده برای نقشه‌برداری مناطق دگرسانی دارای طلا و مس در جنوب گبال‌ام منقول و جبل الخرازه، صحرای شمال شرقی، مصر

عبدالله عاطف[1*]، احمد علی مدنی[1]، عادل عبدالله سرور[1،2] و مخلص کمال آذر[3]

1. گروه زمین شناسی، دانشکده علوم، دانشگاه قاهره، جیزه، مصر
2. گروه علوم زمین شناسی، دانشکده علوم، دانشگاه گالالا، شهر جدید گالالا، مصر
3. گروه علوم زمین شناسی، مرکز تحقیقات ملی، جیزه، دوکی، مصر

ارسال 2023/07/27، پذیرش 2023/09/14

* نویسنده مسئول مکاتبات: abdallah@sci.cu.edu.eg

چکیده:

این مطالعه کاربرد داده‌های سنجش از دور و مدل‌سازی GIS دانش محور را برای ارائه نقشه‌های مطلوبیت برای مناطق معدنی طلا و مس گزارش می‌دهد. جبل جنوبی ام منقول (SGUM) و چشم انداز گابل الخرازه (GKZ) واقع در شمال صحرای شرقی مصر، اهداف مطالعه حاضر هستند. چهار لایه موضوعی (نقشه‌های سنگ‌شناسی، تحلیل بافر ترانشه‌های قدیمی، نقشه‌های چگالی خطی، و نقشه‌های ناحیه تغییر) تهیه و به‌عنوان ورودی برای یک مدل GIS همپوشانی وزنی استفاده شد. نتایج ترکیبی از تصاویر ترکیبی رنگ نادرست، به ویژه پارامترهای RGB (PC2، PC1، و PC3) و پارامترهای RGB (MNF1، MNF2، و MNF3) سنگ‌های میزبان را در هر دو چشم‌انداز طبقه‌بندی کردند. استخراج خطوط خطی مبتنی بر PCA با استفاده از الگوریتم خط PCI Geomatica در نظر گرفته شد. ریاضیات باند (G+B) QuickBird، (R+G) و (G-B) برای RGB در ترسیم کارهای باستانی در مناطق معدنی موفق بود. لایه‌های ترانشه‌های قدیمی به نوارهایی به عرض 20 متر که در همه جهات گسترش یافته بودند، بافر شدند. تصاویر نسبت باند Landsat-8 (5/6 * 5/4، 7/6، و 2/6) در رنگ‌های قرمز، سبز و آبی (RGB) در تعریف مناطق دگرسانی که میزبان کانی‌های طلا و مس هستند، قوی است. نمرات قابل قبول 30٪، 30٪، 20٪ و 20٪ به ترتیب برای نقشه‌های منطقه تغییر، تجزیه و تحلیل بافر کار باستان، نقشه‌های سنگ‌شناسی و نقشه‌های چگالی خط خطی اختصاص داده شد. دو نقشه مطلوبیت برای کانی سازی برای چشم انداز SGUM و GKZ تولید شد. اعتبار سنجی این نقشه‌ها و کاربرد بالقوه آنها برای شناسایی سایت‌های کانی سازی جدید در شمال کویر شرقی مورد بحث قرار گرفت.

کلمات کلیدی: سنجش از دور، تجزیه و تحلیل GIS، کانی‌سازی طلا و مس، نقشه‌های مطلوبیت، روش دانش محور.